Atmos. Chem. Phys., 23, 10661–10675, 2023
https://doi.org/10.5194/acp-23-10661-2023
© Author(s) 2023. This work is distributed under
the Creative Commons Attribution 4.0 License.

Atmospheric Chemistry and Physics
Open Access
EGU

Research article

On the pattern of interannual polar vortex–ozone co-variability during northern hemispheric winter

Frederik Harzer[1], **Hella Garny**[2,1], **Felix Ploeger**[3,4], **Harald Bönisch**[5], **Peter Hoor**[6], **and Thomas Birner**[1,2]

[1]Meteorological Institute, Ludwig-Maximilians-Universität München, Munich, Germany
[2]Institute of Atmospheric Physics, Deutsches Zentrum für Luft- und Raumfahrt, Oberpfaffenhofen, Germany
[3]Institute of Energy and Climate Research, Stratosphere (IEK-7), Forschungszentrum Jülich, Jülich, Germany
[4]Institute for Atmospheric and Environmental Research, University of Wuppertal, Wuppertal, Germany
[5]Institute of Meteorology and Climate Research, Karlsruhe Institute of Technology, Karlsruhe, Germany
[6]Institute for Atmospheric Physics, Johannes Gutenberg University, Mainz, Germany

Correspondence: Frederik Harzer (frederik.harzer@physik.lmu.de)

Received: 20 January 2023 – Discussion started: 13 February 2023
Revised: 29 June 2023 – Accepted: 1 August 2023 – Published: 26 September 2023

Abstract. Stratospheric ozone is important for both stratospheric and surface climate. In the lower stratosphere during winter, its variability is governed primarily by transport dynamics induced by wave–mean flow interactions. In this work, we analyze interannual co-variations between the distribution of zonal-mean ozone and the strength of the polar vortex as a measure of dynamical activity during northern hemispheric winter. Specifically, we study co-variability between the seasonal means of the ozone field from modern reanalyses and polar-cap-averaged temperature at 100 hPa, which represents a robust and well-defined index for polar vortex strength. We focus on the vertically resolved structure of the associated extratropical ozone anomalies relative to the winter climatology and shed light on the transport mechanisms that are responsible for this response pattern. In particular, regression analysis in pressure coordinates shows that anomalously weak polar vortex years are associated with three pronounced local ozone maxima just above the polar tropopause, in the lower to mid-stratosphere and near the stratopause. In contrast, in isentropic coordinates, using ERA-Interim reanalysis data, only the mid- to lower stratosphere shows increased ozone, while a small negative ozone anomaly appears in the lowermost stratosphere. These differences are related to contributions due to anomalous adiabatic vertical motion, which are implicit in potential temperature coordinates. Our analyses of the ozone budget in the extratropical middle stratosphere show that the polar ozone response maximum around 600 K and the negative anomalies around 450 K beneath both reflect the combined effects of anomalous diabatic downwelling and quasi-isentropic eddy mixing, which are associated with consecutive counteracting anomalous ozone tendencies on daily timescales. We find that approx. 71 % of the total variability in polar column ozone in the stratosphere is associated with year-by-year variations in polar vortex strength based on ERA5 reanalyses for the winter seasons 1980–2022. MLS observations for 2005–2020 show that around 86 % can be explained by these co-variations with the polar vortex.

Published by Copernicus Publications on behalf of the European Geosciences Union.

1 Introduction

Atmospheric ozone has manifold effects on human health and ecosystems on Earth (e.g., Barnes et al., 2022). Furthermore, ozone is known to contribute to climate feedbacks due to its radiative properties (IPCC, 2023; WMO, 2022), emphasizing its relevance for atmospheric and climate sciences. For example, Arctic ozone variability was found to substantially impact tropospheric and surface climate (Smith and Polvani, 2014; Calvo et al., 2015; Ivy et al., 2017; Friedel et al., 2022a, b). Diagnostics based on Antarctic ozone depletion have been proposed to improve seasonal forecasts due to robust correlations with the southern annular mode (Son et al., 2013; Bandoro et al., 2014). Moreover, recent studies reported significant effects of CO_2-induced ozone changes on climate sensitivity and on the tropospheric circulation based on models that include interactive ozone (Dietmüller et al., 2014; Nowack et al., 2015, 2018; Chiodo and Polvani, 2017, 2019; Chiodo et al., 2018).

Interannual variability, i.e., variability based on year-by-year anomalies, sheds light on the intrinsic climate fluctuations in the atmosphere and, hence, is essential for understanding long-term trends, e.g., due to external anthropogenic forcings. Several studies exist in the literature that address the relationship between ozone variability and stratospheric dynamics on this timescale. In particular, planetary waves in the stratosphere, resulting from tropospheric wave activity, have been shown to modulate transport and the zonal-mean distribution of ozone (Hartmann and Garcia, 1979; Garcia and Hartmann, 1980). Based on observational data, a case study by Leovy et al. (1985) demonstrated that the concept of wave breaking can be used to explain co-variability between ozone and potential vorticity in the polar vortex region. Kinnersley and Tung (1998) analyzed the impact of the quasi-biennial oscillation and planetary wave anomalies on global ozone. Detailed insights into year-by-year variability in atmospheric ozone from both models and observations were provided in subsequent work, mostly based on the upward Eliassen–Palm flux and meridional eddy heat transport at the 100 hPa level as the metrics for stratospheric wave driving (Fusco and Salby, 1999; Randel et al., 2002; Weber et al., 2003; Ma et al., 2004).

While previous studies primarily focused on variations in column ozone, in this work we draw attention to the vertically resolved pattern of year-by-year ozone variability. To start, consider Fig. 1, which shows maps of local sample standard deviations for zonal-mean ozone relative to the winter climatology, based on detrended seasonal-mean data for northern hemispheric winters (December–February, DJF) from two modern reanalyses (ERA-Interim and ERA5) and MLS satellite measurements. More details on the data used are provided in Sect. 2 below. Although these three datasets show considerable quantitative differences, the three maps consistently show a striking tripole structure over the polar cap with isolated variance maxima near the tropopause, in the middle stratosphere and near the stratopause. In this study, we demonstrate that major parts of this variability structure are congruent with interannual co-variations with the stratospheric polar vortex. To do so, we apply a linear regression approach with the seasonal strength of the polar vortex as the predictor, which is characterized by a simple index time series based on polar-cap-averaged temperature at 100 hPa. We limit our analyses to the Northern Hemisphere since the polar vortex features substantially stronger dynamical variability compared to the Southern Hemisphere. This allows for stronger coupling to ozone transport there. Furthermore, we focus on variations in the polar stratosphere, which are expected to be governed mainly by the Brewer–Dobson circulation, coupled to the variability in polar vortex strength. We find that the resulting winter-mean ozone response pattern may be explained by the combined effects of mixing and residual circulation transport, consistent with previous work focusing on column ozone and the response to sudden stratospheric warmings (e.g., de la Cámara et al., 2018a, b; Hong and Reichler, 2021; Bahramvash Shams et al., 2022).

The paper is structured as follows. In Sect. 2, we list the data used for this study and discuss the setup for the linear regressions. The resulting ozone response patterns are documented in Sect. 3, where we combine regression maps for both pressure and potential temperature coordinates. This allows us to estimate the relative contributions linked to diabatic and adiabatic vertical transport of ozone in the lower polar stratosphere, respectively. In Sect. 4, an ozone budget analysis derived from daily ERA-Interim reanalysis data provides further details on how transport variations produce ozone anomalies at the different levels and regions in the latitude–height plane. Section 5 summarizes our results and provides a brief outlook.

2 Data and methods

For the main part of this study, we use model level output of ERA-Interim reanalyses (Dee et al., 2011) for 1979–2016, which we interpolated on pressure and potential temperature levels such that the full vertical resolution of the model was preserved. With that, we consider zonal-mean data on both pressure and isentropic levels on a vertical range roughly from 1000 to 1 hPa and 260 to 1800 K, respectively, with a meridional resolution of about 0.7°. Monthly means are derived from 6 h daily data and are combined for seasonally averaged fields for December–February (DJF) 1980–2016. Each DJF winter season is denoted with the year of the corresponding January month.

Detailed assessments show that ERA-Interim (ERAI) ozone in the lower stratosphere is in reasonable agreement with observations and other reanalysis products (Dragani, 2011; Albers et al., 2018; Davis et al., 2022). We intend to provide further validation by comparing our results obtained from ERAI on pressure levels with those based on the lat-

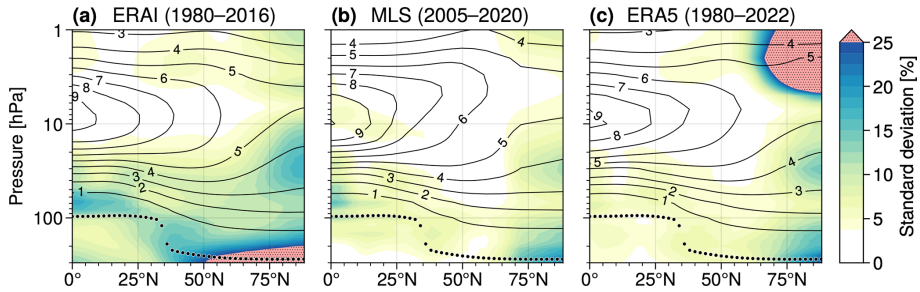

Figure 1. Maps of ozone variability (DJF), based on local sample standard deviations relative to the ozone DJF climatology (shown by the solid contour lines in units of parts per million by volume), for ERA-Interim (ERAI), MLS and ERA5. The thick dotted lines show the mean thermal tropopause derived from ERAI data. For ERAI and ERA5, extreme ozone variations (indicated by red shading and stippling) are caused by outliers. Note that throughout this study, thermal tropopause heights are calculated using PyTropD (Adam et al., 2018), following the definition by WMO (1957).

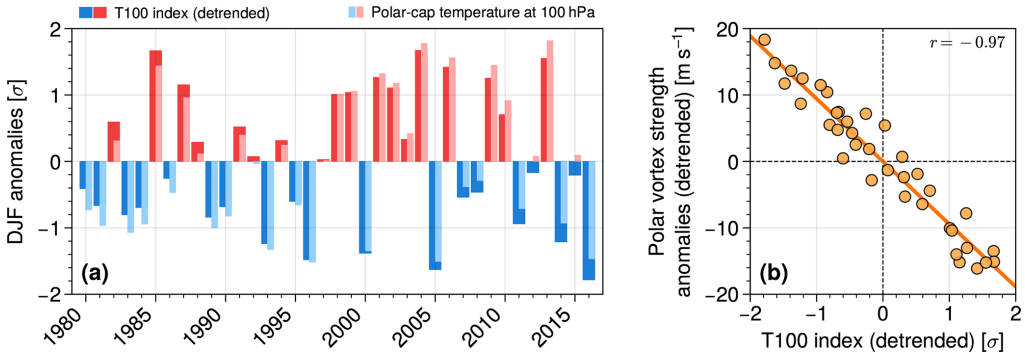

Figure 2. **(a)** T100 index obtained from ERAI reanalysis data, adjusted for a linear trend in time as required for the linear regression approach. The underlying polar-cap-averaged temperature anomalies at the 100 hPa level, without this trend removed, are shown by the thin bars. Both time series are standardized by the standard deviation of the T100 index, $\sigma = 2.6\,\mathrm{K}$. **(b)** Interannual anomalies of the zonal-mean zonal wind at the polar vortex around 60° N and 10 hPa, regressed on the T100 index with a regression coefficient $b = -9.4\,\mathrm{m\,s^{-1}}\,\sigma^{-1}$ and correlation $r = -0.97$. All results are for ERAI, DJF 1979/80–2015/16.

est ERA5 reanalyses for DJF 1960–2022 with regular 1.5° meridional grid spacing (Hersbach et al., 2019, 2020; Bell et al., 2021). ERA5 data for the pre-satellite era, covering DJF 1960–1980, will be evaluated separately. In addition, we use ozone observations from the Microwave Limb Sounder (MLS) instrument on board the Aura satellite, data version 5 (Waters et al., 2006; Livesey et al., 2022). The spatial sampling of MLS is comparatively high, with about 3500 profiles along about 15 orbits per day, covering the globe between about 82° S and 82° N. The MLS profile data have been interpolated on potential temperature levels, and monthly mean zonal-mean climatologies have been compiled for both pressure and potential temperature levels. In this paper, MLS data are considered on pressure levels for DJF 2005–2020 on a non-regular latitudinal grid with mean resolution of approx. 4.2°.

Throughout this study, correlations are measured by using local Pearson correlation coefficients r and p values are calculated using a two-sided Wald t test. Statistical significance is assumed if $p \leq 0.05$. The correlation coefficients' 95 % confidence intervals are computed based on Fisher's z transformation.

Co-variability between stratospheric ozone and polar vortex strength is studied by using a simple linear least-squares regression model: first, we define an index time series that is derived from interannual zonal-mean temperature, interpolated at the 100 hPa pressure level and averaged over the Northern Hemisphere's polar cap,

$$\overline{T}_{100}(t) \equiv \left\langle \overline{T}(t, p = 100\,\mathrm{hPa}, \phi) \right\rangle_{\phi \geq 60^\circ\,\mathrm{N}}, \tag{1}$$

which we will refer to as "T100 index" in the following. Here, overbars indicate the zonal mean and squared brackets denote meridional averaging. The relation between the T100 index and polar vortex strength variability is discussed below within the context of atmospheric dynamics. Then, for a given variable field $\overline{y}$, the corresponding anomalies $\delta\overline{y}$ are regressed on this index according to

$$\delta\overline{y}(t) = a + b \cdot \overline{T}_{100}(t) + \epsilon(t). \tag{2}$$

For both the index and the anomaly time series, potential linear trends across the whole time range under consideration

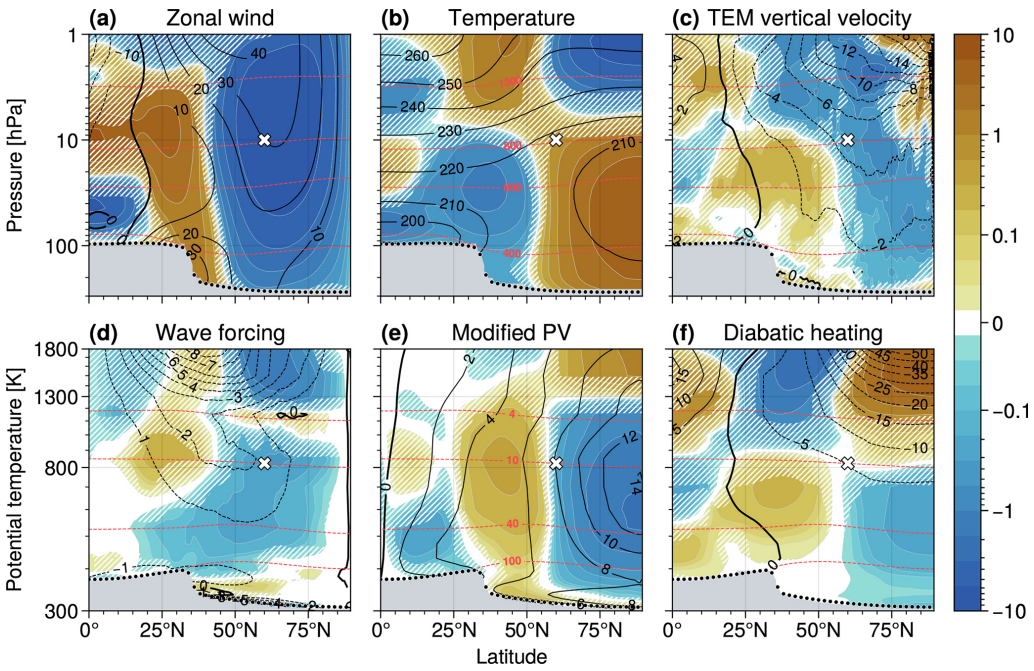

Figure 3. Interannual anomalies of the zonal-mean **(a)** zonal wind (in units of $\mathrm{m\,s^{-1}}$), **(b)** temperature (K), **(c)** TEM vertical velocity in log-p coordinates ($\mathrm{km\,month^{-1}}$), i.e., $W_\mathrm{r} = -(H/p)\omega_\mathrm{r}$ with scale height $H = 7\,\mathrm{km}$ and ω_r from Eq. (3), **(d)** PV flux $\overline{\hat{v}\sigma\hat{q}}\cos\phi$ (in $\mathrm{m\,s^{-1}\,d^{-1}}$) as a diagnostic for adiabatic wave forcing (Tung, 1986), **(e)** modified PV $\overline{\Pi}^* \equiv \overline{q}^*(\theta/\theta_0)^{-9/2}$ in units of $1\,\mathrm{PVU} = 1\times10^{-6}\,\mathrm{K\,m^2\,kg^{-1}\,s^{-1}}$ (Lait, 1994), with density-weighted PV $\overline{q}^*$ and $\theta_0 = 350\,\mathrm{K}$ and **(f)** diabatic heating $\overline{Q}^*$ ($\mathrm{K\,d^{-1}}$), regressed on the standardized ERAI T100 index. The regression maps are visualized by the color shading and measured per standard deviation of the index. Note that the panels in the first and second row show the results for pressure and isentropic coordinates, respectively. Hatches indicate where the regressions are not statistically significant. Contour lines show the DJF climatologies of the input fields. The approximate position of the polar vortex around 60° N and 10 hPa is shown by the white markers. The thick dotted lines represent the mean thermal tropopause for DJF. Dashed red lines show selected isentropes (in Kelvin, **a–c**) and isobars (in hectopascals, **d–f**), respectively. Note uneven color contour intervals with linear spacing for values within ±0.1 and logarithmic spacing outside that range. All results are based on ERAI, DJF 1980–2016. Data assimilation and model approximations may cause inconsistencies in the results, which is the case, e.g., for the TEM vertical velocity in **(c)** below the polar stratopause compared to the responses of temperature and diabatic heating in panels **(b)** and **(f)**, respectively.

are identified through separate linear least-squares regressions and removed beforehand. Finally, the set of regression coefficients $b(p,\phi)$ yields a "T100 regression map" across the latitude–height plane that quantifies the statistical linear response of $\overline{y}$ if polar stratospheric temperature, measured by the standardized T100 index, is varied by 1 standard deviation. In this work, this regression model is primarily applied to zonal-mean year-by-year anomalies covering DJF winter seasons on the Northern Hemisphere. When daily anomalies are considered, the procedure is similar except that in addition the time series are deseasonalized beforehand.

The detrended and standardized T100 index derived from ERAI reanalyses for DJF 1980–2016 is provided in Fig. 2a. Choosing this T100 predictor for studying polar vortex co-variability is justified due to its strong dependence on variations in the zonal wind in the polar vortex region at 60° N and 10 hPa, as shown in Fig. 2b. We therefore obtained a well-defined and powerful proxy diagnostic for the strength of the polar vortex during northern hemispheric winters. Based on temperature as a fundamentally constrained variable instead of zonal wind, this definition features a robust T100 time series across other selected reanalysis products and for moderate changes in the pressure level at which this index is evaluated (not shown).

The polar-cap lower-stratospheric temperature and the strength of the polar vortex are coupled via downward control (Haynes et al., 1991). Some important variable fields, which are intended to illustrate this mechanism, and their T100 regression maps are provided in Fig. 3. Briefly, starting with anomalously strong wave activity of tropospheric origin, westerly winds in the polar vortex region are reduced (as shown in Fig. 3a) upon enhanced wave dissipation, inducing a wave-driven poleward residual flow that counteracts the weakening of the background zonal wind due to the Coriolis effect. The wave forcing is indicated by enhanced equatorward potential vorticity (PV) fluxes around the 800 K isentrope in Fig. 3d, which reduce PV above the polar cap (Fig. 3e). The associated temperature response in Fig. 3b is consistent with thermal wind balance. Downwelling (upwelling) is associated with adiabatic warming (cooling), such

that by continuity this closes the anomalous residual circulation. This vertical motion (shown with log-p scaling in Fig. 3c) is captured in the transformed Eulerian mean (TEM) framework by (e.g., Andrews et al., 1987)

$$\overline{\omega}_{\mathrm{r}} = \overline{\omega} + \frac{1}{a\cos\phi\,\partial_p\overline{\theta}}\partial_\phi\left(\overline{v'\theta'}\cos\phi\right), \tag{3}$$

where $\overline{\omega} = \mathrm{d}p/\mathrm{d}t$ is the vertical velocity in pressure coordinates, $\overline{\theta}$ denotes zonal-mean potential temperature, $\overline{v'\theta'}$ indicates the meridional eddy heat transport and a is the Earth's radius. The change in potential temperature due to diabatic heating in Fig. 3f can be consistently explained to damp the wave-driven temperature perturbations through radiative cooling.

The underlying mechanism has been widely discussed in studies on stratosphere–troposphere coupling, where the T100 index described above has been introduced (Baldwin et al., 2019; Domeisen et al., 2020). On sub-seasonal timescales, similar effects are observed, e.g., during sudden stratospheric warmings (Butler et al., 2017; Baldwin et al., 2021).

Previous studies often referred to the meridional eddy heat transport at 100 hPa as an indicator for the total available wave driving of the stratosphere (e.g., Fusco and Salby, 1999; Randel et al., 2002; Ma et al., 2004; Weber et al., 2003, 2011; Strahan et al., 2016). However, it is unclear how this wave driving manifests in terms of its latitude–height structure. Furthermore, this metric is more complex than the T100 index, such that it may be less robust across different data products. Following Weber et al. (2011), we used the zonal-mean meridional eddy heat flux $\overline{v'T'}$ at 100 hPa averaged between 45 and 75° N ("VT100 index") from ERAI reanalyses and briefly assessed the resulting signature for ozone co-variability (DJF, 1980–2016). From a regression analysis, we found clear similarities in the response patterns obtained for the T100 DJF (discussed below) and the VT100 NDJ (November–January, see Appendix A) time series. This time lag between the T100 and VT100 predictors consistently supports the interpretation of anomalous eddy heat fluxes that precede wave-induced deceleration of the polar vortex by several weeks (Newman et al., 2001; Polvani and Waugh, 2004).

3 Polar vortex–ozone co-variability: T100 response patterns

In the lower stratosphere, it is mainly the Brewer–Dobson circulation (BDC) that captures ozone transport from the tropics towards higher latitudes (Gettelman et al., 2011; Butchart, 2014). Since wave forcing impacts the strength of both the polar vortex and the BDC, an anomalously weak polar vortex tends to be associated with enhanced poleward ozone transport and, hence, increased polar ozone amounts. Previous studies reported strong coupling between the strength of the BDC and stratospheric temperature (Fu et al., 2010; Weber et al., 2011; Young et al., 2012), which suggests substantial interannual co-variability between the T100 diagnostic and stratospheric ozone. In this section, we aim to document this T100 ozone response pattern and provide a comparison based on two different perspectives, i.e., using pressure and potential temperature as the vertical coordinate, respectively.

First, Fig. 4 shows zonal-mean ozone volume mixing ratios $\overline{\chi}$ on pressure levels, from ERAI and ERA5 reanalysis data as well as from MLS observations, regressed on the standardized ERA5 T100 index. This index represents an extended (available for DJF 1980–2022) but essentially equivalent version of the ERAI T100 time series due to its outstanding high correlation, $r > 0.99$. The regression maps are provided in relative units, based on the corresponding ozone DJF climatology, and per standard deviation of the T100 time series. The stratospheric response signatures show very good agreement among the different datasets in Fig. 4. This is especially worth noting due to the substantial differences in the strength of general ozone variability in Fig. 1. From a more detailed analysis, robust results were found for other selected reanalysis products and for modern chemistry–climate models (not shown; see also von Heydebrand, 2022).

In general, Fig. 4 supports the idea that higher ozone amounts over the polar cap are related to anomalously strong poleward transport due to a stronger BDC during weak polar vortex years. This is consistent with the diabatic heating response in Fig. 3f that suggests anomalous upwelling (downwelling) in lower (higher) latitudes for ERAI and, hence, a stronger stratospheric residual circulation. Moreover, the results reflect the vertical structure of year-by-year ozone variability, featuring those three pronounced variance maxima above the polar cap previously discussed with Fig. 1. In addition, the T100 regression maps show another spot of enhanced ozone in the mid-latitudes slightly below the 100 hPa level, which is roughly between the two lowest polar response maxima.

To understand these features, we gain some first insights from just evaluating the differences among the response signatures obtained for pressure and potential temperature as the vertical coordinate. For this, consider Fig. 5, which shows the T100 regression maps for zonal-mean ozone $\overline{\chi}$ on pressure levels (top row) and density-weighted ozone, $\overline{\chi}^* = \overline{\rho_\theta \chi}/\overline{\rho_\theta}$ with isentropic density $\rho_\theta = g^{-1}\partial_\theta p$, for potential temperature coordinates (bottom row). Both computations were obtained from ERAI reanalysis data for DJF 1980–2016. For comparison, the response signatures are displayed not only in relative units (right column) but also as absolute anomalies in parts per million by volume (left column), $1\,\mathrm{ppmv} = 1\times10^{-6}\,\mathrm{mol\,mol^{-1}}$.

The results show clear differences among the two coordinate frameworks, which shed light on some relevant transport processes that build up this ozone response signature. For example, consider the two upper polar response max-

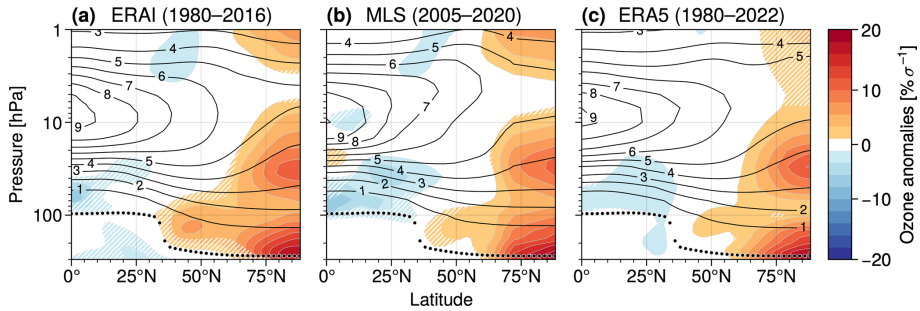

Figure 4. Interannual zonal-mean ozone on pressure levels from **(a)** ERAI (DJF 1980–2016), **(b)** MLS (2005–2020) and **(c)** ERA5 (1980–2022), regressed on the standardized ERA5 T100 index. The response signatures are provided as relative anomalies (in $\%\,\sigma^{-1}$) based on the respective ozone DJF climatology that is shown by the black contour lines each (in parts per million by volume). The thick dotted lines show the mean thermal tropopause for DJF, derived from ERAI. Other details as in Fig. 3.

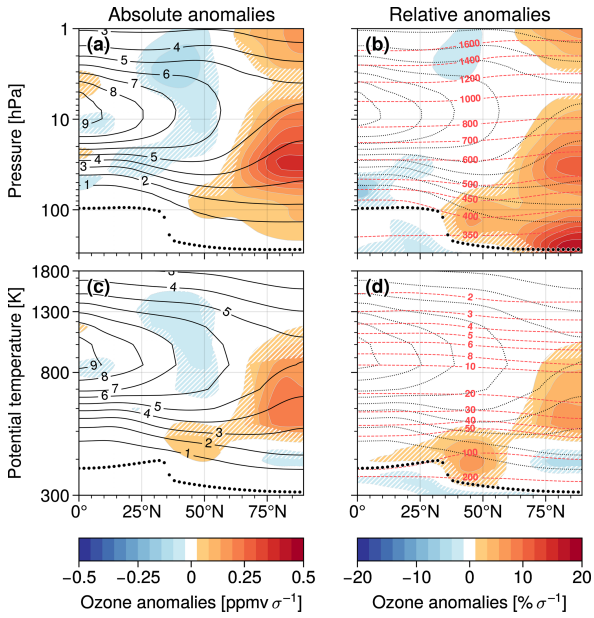

Figure 5. **(a)** T100 regression map for anomalous zonal-mean ozone $\overline{\chi}$ on pressure levels (ERAI, DJF 1980–2016). **(b)** Same as in **(a)** but the response signature is given by relative anomalies with respect to the DJF ozone climatology. (**c** and **d**) Corresponding T100 regression maps for density-weighted zonal-mean ozone on potential temperature levels, $\overline{\chi}^* = \overline{\rho_\theta \chi}/\overline{\rho_\theta}$, where ρ_θ is isentropic density. Details as in Fig. 4.

ima around 1 and 30 hPa, respectively, and the corresponding minima at similar altitudes around 40° N, more pronounced in the absolute anomalies (top row in Fig. 5). We expect them to arise due to the quadrupole-like response in temperature and TEM vertical velocity (Fig. 3b and c), associated with the anomalously weak polar vortex in Fig. 3a. The sign of the ozone response directly follows from the anomalous up- and downwelling acting on the local vertical gradient of the background ozone distribution. In contrast, this response is much weaker in potential temperature coordinates (bottom row in Fig. 5). This is because vertical ozone transport includes a component due to adiabatic motion, which satisfies $\mathrm{d}\theta/\mathrm{d}t = 0$ and which can be thought of as shifting the isosurfaces of both ozone and potential temperature simultaneously. Thus, for vertical transport, unlike the diabatic part, the adiabatic proportion is implicitly accounted for in isentropic coordinates. Konopka et al. (2009) used similar arguments to explain differences in the amplitude of the seasonal cycle of tropical ozone when viewed in pressure and isentropic coordinates.

In the lowermost stratosphere just above the polar tropopause, we find the most remarkable differences among the results for the two coordinate systems used in Fig. 5. Regarding pressure levels, from Fig. 5b we find a pronounced ozone response maximum with relative anomalies of more than $15\,\%\,\sigma^{-1}$. Using potential temperature as the vertical coordinate, we instead obtain a decrease in ozone there in Fig. 5d, suggesting that anomalous downwelling (shown in Fig. 3c) contains a much larger adiabatic component there compared with higher stratospheric regions. This is consistent with smaller radiative damping rates that are observed in the lower polar stratosphere and that limit the effectiveness of diabatic cooling (Hitchcock et al., 2010).

The large differences between pressure and isentropic coordinates in the lowermost stratosphere are also apparent when considering variations in the polar-cap tropopause (Fig. 6): tropopause pressure shows a much larger response to T100 variability (by about a factor of 10) than potential temperature, indicating that polar tropopause height variability is mainly governed by adiabatic processes. Significantly enhanced ozone then is observed where the substantial lowering of the tropopause height allows for downward transport of stratospheric ozone into former tropospheric regions, which is the case for pressure rather than potential temperature coordinates. As a result, enhanced ozone is found at the polar tropopause in Fig. 5b, where relative anomalies occur that are large compared to the low ozone amounts usually expected in the upper troposphere.

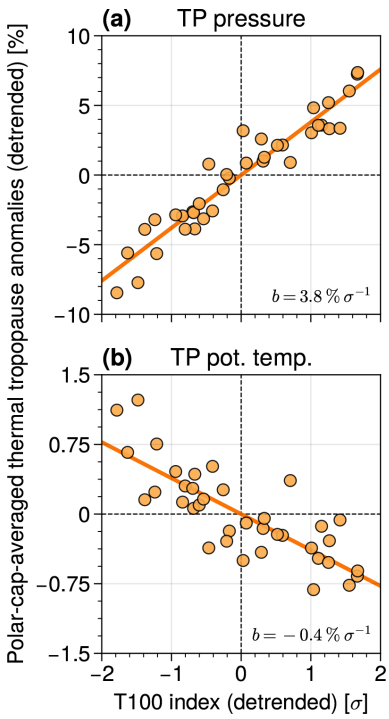

Figure 6. **(a)** Polar-cap-averaged thermal tropopause (TP) pressure regressed on the T100 index (ERAI, DJF 1980–2016), with slope $b = 3.8\,\%\,\sigma^{-1}$ from a linear least-squares fit and correlation $r = 0.95$. Much less co-variability is found in **(b)** for polar-cap TP potential temperature ($r = -0.80$).

Taking into account comprehensive research by de la Cámara et al. (2018a, b) on anomalous stratospheric dynamics and Arctic ozone during sub-seasonal sudden stratospheric warming events, we hypothesize that the remaining T100 response signatures in Figs. 4 and 5 can be explained through variations in the BDC, combining the effects of residual-mean (net mass) downwelling and quasi-isentropic eddy mixing, depending on the local gradients of stratospheric ozone. Within this context, analyzing the full ozone budget turned out to be appropriate for investigating the actual roles of these transport contributions.

4 Insights into polar vortex–ozone co-variability from the ozone budget

Using isentropic coordinates, the zonal-mean ozone budget reads (e.g., Andrews et al., 1987; Plumb, 2002)

$$\partial_t \overline{\chi}^* + \underbrace{\frac{\overline{v}^*}{a}\partial_\phi \overline{\chi}^*}_{-①} + \underbrace{\overline{Q}^* \partial_\theta \overline{\chi}^*}_{-②} = -\overline{\rho_\theta}^{-1}\left[\underbrace{\frac{1}{a\cos\phi}\partial_\phi\left(\overline{\hat{v}\rho_\theta\hat{\chi}}\cos\phi\right)}_{③} + \underbrace{\partial_\theta\overline{\hat{Q}\rho_\theta\hat{\chi}}}_{④}\right] + \overline{S}^*. \quad (4)$$

Here, χ denotes the ozone volume mixing ratio, $Q = \mathrm{d}\theta/\mathrm{d}t$ is the change in potential temperature due to diabatic heating, $\rho_\theta = g^{-1}\partial_\theta p$ is isentropic density and S represents sources and sinks. We use a density-weighted zonal average, $\overline{\chi}^* \equiv \overline{\rho_\theta \chi}/\overline{\rho_\theta}$, with $\hat{\chi} = \overline{\chi} - \overline{\chi}^*$ indicating deviations therefrom and spherical coordinates with geographical latitude ϕ and Earth's radius a. The tendencies induced by mean flow advection and by eddy mixing are accounted for by the terms ①+② and ③+④, respectively.

Figure 7 provides the T100 regression maps for the relevant dynamical fields and their associated ozone tendencies. We have neglected the contributions due to the mean meridional flow and due to vertical eddy ozone transport, numbered with ① and ④ in Eq. (4), since they are small compared to the other processes (not shown). We further omit contributions to ozone variability due to chemistry, i.e., $S \approx 0$ in Eq. (4), which is typically fulfilled in the lower stratosphere. Under very cold conditions, however, ozone depletion may still become important there (e.g., Brasseur and Solomon, 2005). Contributions due to chemistry cannot be neglected in the upper stratosphere; we therefore limit our budget analysis to lower-stratospheric regions, such that $\theta < 900\,\mathrm{K}$ in Fig. 7.

The results show that pronounced anomalous ozone tendencies are mainly found between 400 and 700 K, where anomalous diabatic vertical transport above the polar cap brings ozone-rich air to lower altitudes, whereas quasi-isentropic eddy mixing counteracts this response by transporting ozone from the polar region to the mid-latitudes. Moreover, Fig. 7d and e show that these two leading contributions to ozone variability, ② and ③ as labeled in Eq. (4), are largest around 500 K, reflecting the interplay between background ozone gradients and the circulation changes caused by anomalous wave forcing in the polar vortex region according to Fig. 7c. We furthermore note that, especially in higher latitudes, these anomalous contributions ② and ③ largely compensate for each other. Indeed, the residual ozone tendency is expected to be small, since individual seasonal averages should be approximately in steady state. However, the polar-cap-averaged vertical profiles of the responses in Fig. 7f show clear differences in the absolute strength of these anomalies, suggesting an imbalance of the seasonal-mean ozone budget instead, especially near 500 K, where the resulting net tendency is negative, $\partial_t \overline{\chi}^* \approx ② + ③ < 0$. This may seem to contradict the enhanced seasonal-mean ozone that is found there during weak polar vortex years (e.g., compare Fig. 5c). However, a seasonal-mean net negative tendency would merely state that lower ozone values are found at the end compared to the beginning of the season, but this would still allow for strong positive ozone anomalies during the season. Moreover, the actual diagnosed seasonal-mean net ozone tendency is in fact slightly positive near 500 K (not shown), which indicates that the detailed quantitative balance of the contributions due to diabatic downwelling and quasi-isentropic eddy mixing is not accurately reproduced in ERAI. This is consistent with Fig. 4, which shows higher

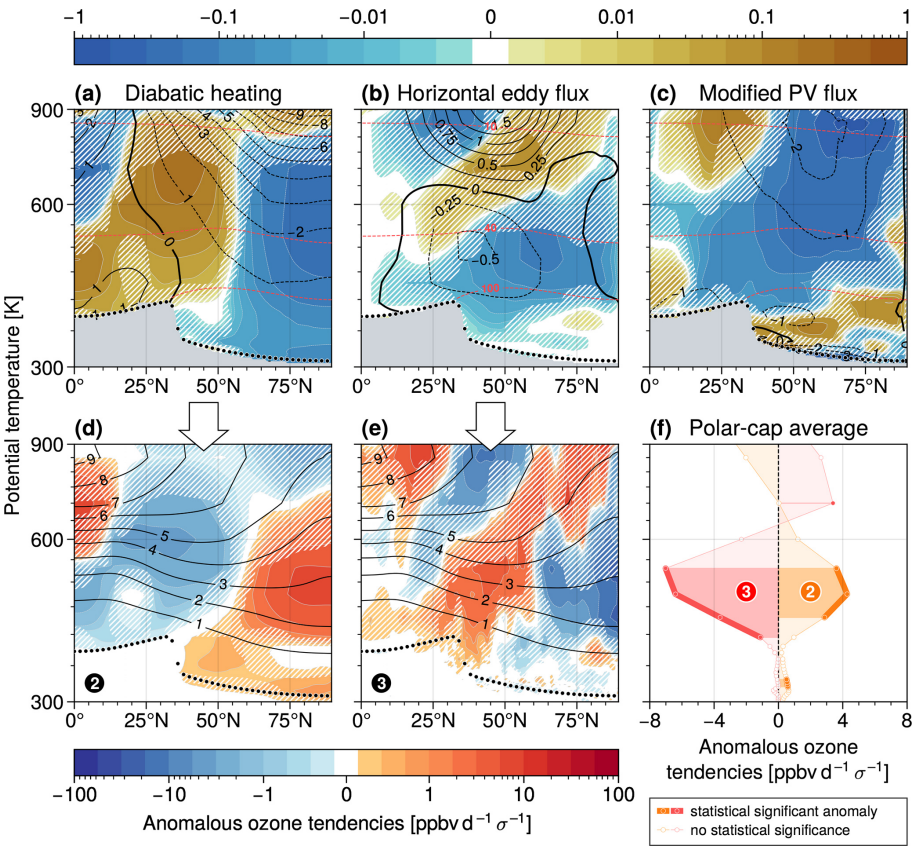

Figure 7. **(a)** Anomalous diabatic heating rates $\overline{Q}^*$ (in K d^{-1}) and **(b)** horizontal eddy ozone transport $\overline{\hat{v}\rho_\theta\hat{\chi}}/\overline{\rho_\theta}$ (in ppmv m s^{-1}) regressed on the T100 index (ERAI). **(c)** The corresponding regression map for the modified PV flux $\overline{\hat{v}\rho_\theta\hat{\Pi}}/\overline{\rho_\theta}$ (in PVU m s^{-1}) is added for comparison. Details as in Fig. 3. (**d** and **e**) T100 regression maps for the anomalous tendencies ② and ③ from Eq. (4). Here, the black contours show the ozone DJF climatology (in parts per million by volume). Note uneven color contour intervals with linear spacing for values within ±0.01 **(a–c)** and ±1 ppbv d^{-1} σ^{-1} (**d** and **e**), respectively, and logarithmic spacing outside those ranges. The anomalous ozone tendencies seem to be weak in the lowermost stratosphere and increase strongly for altitudes higher than 400 K due to increased wave forcing above that isentrope as indicated by the anomalous equatorward PV fluxes in **(c)**. Weak positive ozone tendencies due to enhanced diabatic cooling directly above the tropopause in **(d)** probably arise from an increase in static stability there, e.g., as observed for sudden stratospheric warmings (Grise et al., 2010; Son et al., 2011; Wargan and Coy, 2016) or can be explained as a second-order feedback reacting to changes in the vertical ozone gradients. **(f)** Polar-cap-averaged tendencies, $\langle\partial_t\overline{\chi}^*\rangle_\phi$ for $\phi \geq 60°$ N, regressed on the ERAI T100 index. Thick solid lines mark isentropes with statistically significant anomalies. All results are for ERAI, DJF 1980–2016.

ozone anomalies in mid-latitudes in ERAI compared to MLS and ERA5, presumably due to excessive horizontal mixing.

These findings need to be treated with caution. In particular, uncertainties in the ERA-Interim reanalyses remain due to data assimilation and due to parameterization of interactive ozone and the associated feedbacks (Davis et al., 2022). Furthermore, diabatic heating rates are solely derived from the model forecasts without any additional constraints and, hence, can introduce additional budget inconsistencies (e.g., Abalos et al., 2015; Monge-Sanz et al., 2022). In conclusion, we do not expect the ozone budget to be closed in ERA-Interim. The cumulative nature and the smaller magnitudes of the winter-mean tendencies may be even more challenging in that respect. We therefore think that such uncertainties only allow for a rather qualitative estimate of the different ozone transport processes. Additional work is needed to compare these results with other reanalysis products, observational data and model simulations. Limited to the data available from ERA-Interim, we did not find a robust response profile for the resulting net tendency that follows from the anomalous tendencies ②+③ in Fig. 7f; i.e., statistical significance (if any) is sensitive to the latitude range chosen for polar-cap averaging (not shown). This suggests that the full seasonal-mean ozone budget may indeed be balanced, such that the T100 response of the net tendency $\partial_t\overline{\chi}^* \approx ② + ③$ in Eq. (4) vanishes for seasonal averages, assuming that ozone chemistry $\overline{S}^*$ does not play a dominant role in the lower stratosphere.

At this point, the contrasting results presented above complicate reliable conclusions on the underlying transport dy-

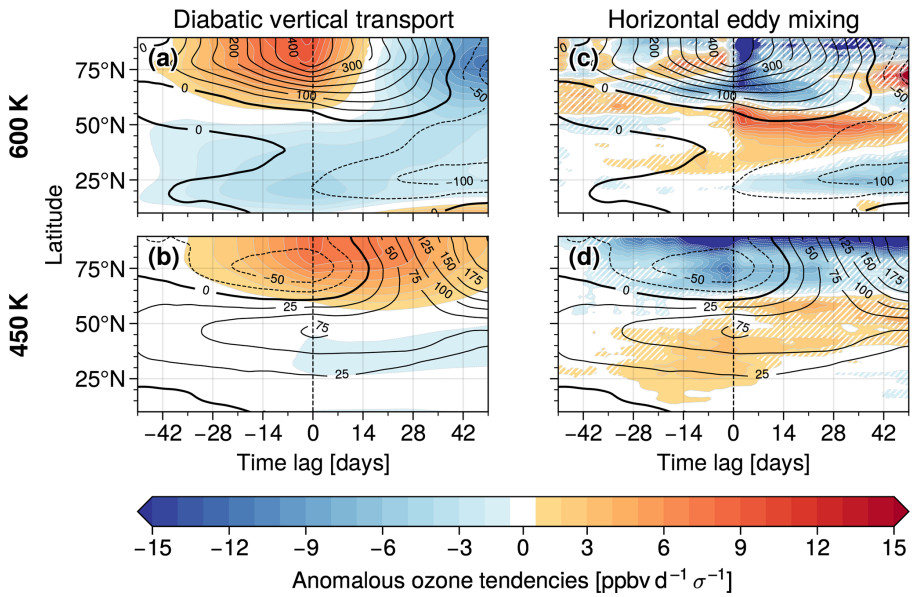

Figure 8. Anomalous ozone tendencies associated with **(a** and **b)** diabatic heating, ② in Eq. (4), and **(c** and **d)** horizontal eddy mixing ③, respectively, regressed on daily T100 anomalies on the 600 K **(a** and **c)** and 450 K **(b** and **d)** isentropes. Evaluation of a robust positive response at 600 K associated with anomalous diabatic mean flow advection in the tropics (not shown), which occurred across all the lag times considered here and possibly includes the response of the quasi-biennial oscillation, remains for subsequent work. Positive (negative) lag times indicate that the field anomalies succeed (precede) the T100 index. Hatching indicates where co-variability is not statistically significant. Black contour lines illustrate T100 lag regressions for daily ozone anomalies $\overline{\chi}^*$ in parts per billion by volume per standard deviation of the daily T100 index. All results are for deseasonalized daily mean ERAI data, covering December, January and February months in 1979–2016.

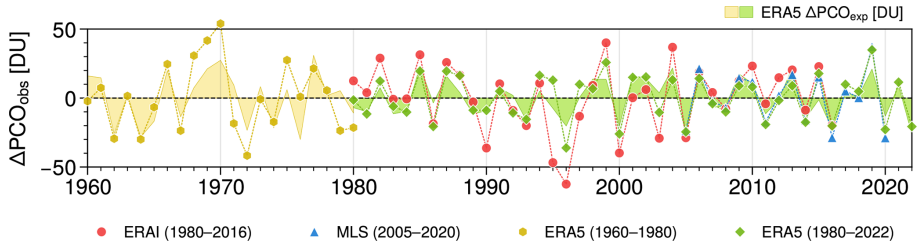

Figure 9. Observed polar-cap-averaged partial column ozone anomalies ΔPCO_{obs} per DJF winter season (line plots) for ERAI, MLS and ERA5 data and, for comparison, explained partial column ozone ΔPCO_{exp} for ERA5 (area plots). See the text for details on the computation.

namics based on winter-mean ozone tendencies. Instead, to reveal more insights into the drivers of the seasonal-mean ozone anomalies, it is useful to study daily variability where the relevant transport contributions may not fully compensate one another, leaving a net ozone tendency that allows for better distinguishing cause and effect. To do so, we perform a linear lag-regression analysis using daily averaged fields based on 6 h ERAI data for the December, January and February months in 1979–2016. We select two isentropes, 600 and 450 K, which represent the polar ozone response maximum and minimum, the latter located beneath the former in Fig. 5c, and assess T100 co-variability for daily ozone and the two relevant dynamical tendencies, ② and ③ in Eq. (4). The results for different lag times, covering 14 weeks in total centered around the T100 anomaly, are shown in Fig. 8. They are consistent with ozone transport taking place, e.g., during sub-seasonal sudden stratospheric warming (SSW) events (de la Cámara et al., 2018a, b; Hong and Reichler, 2021), though here we present lag regressions for the more general case of daily T100 temperature anomalies, which allows for improved statistics and reduced sensitivity, e.g., on SSW definition thresholds. In Fig. 8, for the 600 K isentrope, we find that enhanced polar ozone is mainly induced by anomalous diabatic mean flow downwelling (for negative lag times in Fig. 8a). Subsequently, a reduction in polar ozone takes place due to increased quasi-horizontal eddy mixing in Fig. 8c out of the polar cap toward mid-latitudes, which partly arises as feedback due to strengthened meridional ozone gradients. Concerning the 450 K level, it turns out that the temporal order of the tendencies involved

is now reversed: here, horizontal eddy mixing can be clearly identified to force the negative ozone response in the polar region. This also explains the positive ozone anomaly in the mid-latitudes shown in Fig. 5b and d. Figure 8a and b indicate the anomalies in diabatic mean flow advection propagating downward with time, where they counteract the eddy forcing in lower altitudes. A closer analysis of variations in the underlying wave driving giving rise to anomalous transport, including different contributions due to different parts of the wave spectrum, is beyond the scope of the current analyses and is left for future work.

Overall, our findings here confirm that the complex ozone response signature in the middle stratosphere introduced in Sect. 3 can be explained by the combined effects of horizontal eddy mixing and vertical mean flow advection. The T100 response on sub-seasonal timescales shows significant anomalous ozone tendencies, which consistently explain the variations in seasonal-mean stratospheric ozone but at the same time seem to not influence ozone net tendency on a seasonal scale. The key for this to happen is the two dominant mechanisms of ozone transport that induce competing response tendencies but occur with some temporal distance.

5 Discussion and conclusions

In this paper, we discussed interannual co-variability between the strength of the polar vortex, as indicated by the index time series of polar-cap-averaged temperature at 100 hPa, and zonal-mean ozone during northern hemispheric winters. We focused on the vertically resolved ozone response pattern in the latitude–height plane, which as far as we know has received only little attention in the literature. In particular, we assessed the intriguing ozone response structure in middle and high latitudes across different altitude levels from two different coordinate perspectives: in pressure coordinates, an anomalously weak vortex is associated with increased ozone volume mixing ratios throughout the stratosphere, showing relative maxima just above the polar tropopause, in the lower-to-middle stratosphere and near the stratopause. Using potential temperature as the vertical coordinate, increased ozone is only present in lower altitudes roughly below 900 K and above about 450 K, even showing weakly decreased values in the lowermost stratosphere beneath for ERAI data. We rationalize these disparate ozone variations by a combination of variability in wave-driven quasi-horizontal mixing and vertical advection by the residual circulation. In particular,

1. wave-driven anomalous adiabatic up- and downwelling in the polar vortex region cause enhanced polar ozone around 1 and 30 hPa, as well as less ozone equatorwards,

2. increased downwelling associated with an anomalously weak polar vortex includes a large adiabatic component and acts to simultaneously shift iso-surfaces of potential temperature and ozone also in the lowermost stratosphere, which furthermore results in a lowered tropopause and significantly increased ozone concentrations there, and

3. the ozone response signature in the middle stratosphere can be explained by consecutive counteracting anomalous tendencies associated with diabatic downwelling and quasi-isentropic eddy mixing on daily timescales, with varying chronological order depending on altitude.

Our results consistently show that interannual ozone variations are governed by similar dynamical processes as sub-seasonal ozone variability (see, e.g., Lubis et al., 2017; de la Cámara et al., 2018a, b; Hong and Reichler, 2021; Bahramvash Shams et al., 2022). Moreover, the T100 ozone response pattern clearly reflects the underlying ozone transport anomalies when viewed in the latitude–height plane with a vertically resolved response structure. Similar anomaly signatures are observed during Eastern Pacific El Niño events (Benito-Barca et al., 2022, see, e.g., their Fig. 1g). They have furthermore been obtained from modern CMIP6 climate projections based on various climate forcing scenarios (Match and Gerber, 2022, e.g., their Fig. 1).

Finally, referring back to our initial motivation, we found clear similarities between polar vortex–ozone co-variability and year-by-year variability in zonal-mean ozone in general, as measured by the local sample standard deviation provided in Fig. 1. We may ask to what extent this allows us to constrain polar ozone anomalies during northern hemispheric winters. To do so, we consider seasonal-mean ozone for DJF from ERAI, MLS and ERA5, each interpolated on equidistant pressure levels between 1 and 300 hPa with 1 hPa vertical resolution and adjusted for linear trends across the corresponding time intervals. The observed variability in polar-cap-averaged partial column ozone (PCO) then reads

$$\Delta\mathrm{PCO}_{\mathrm{obs}}(t) = \left\langle \int_{1\,\mathrm{hPa}}^{300\,\mathrm{hPa}} \delta\overline{\chi}(t,p,\phi)\,\mathrm{d}p \right\rangle_{\phi\geq 60^\circ\,\mathrm{N}} . \tag{5}$$

Based on the associated T100 regression map for ozone in the latitude-pressure plane, we reconstruct the variations that are explained by co-variability with the polar vortex,

$$\Delta\mathrm{PCO}_{\mathrm{exp}}(t) = \overline{T}_{100}(t)\cdot \left\langle \int_{1\,\mathrm{hPa}}^{300\,\mathrm{hPa}} b(p,\phi)\,\mathrm{d}p \right\rangle_{\phi\geq 60^\circ\,\mathrm{N}} , \tag{6}$$

corresponding to the general T100 index time series modulated by a constant prefactor that depends on the individual model realization. Finally, the correlation between these two PCO anomaly time series provides a measure for the variance of $\Delta\mathrm{PCO}_{\mathrm{obs}}$ that is associated with seasonal polar vortex strength anomalies. The results obtained for ERAI, MLS and ERA5 are shown in Fig. 9 and Table 1, which are

Table 1. Variances of observed polar-cap-averaged partial column ozone, ΔPCO_{obs}, as defined in Eq. (5), explained by interannual variability in PCO_{exp} from Eq. (6) associated with T100 anomalies. This table extends the results presented in Fig. 9. Explained variances are provided as the squared correlation coefficients obtained from least-squares linear regressions, where minimum and maximum values were derived from the corresponding 95 % confidence intervals for the correlation coefficients based on Fisher's z transformation.

Dataset	Time range	Explained variance [%]		
		min	r^2	max
ERAI	1980–2016	28	53	72
ERA5		48	69	83
	1960–1980	21	55	79
	1980–2022	53	71	83
	2005–2020	47	78	92
MLS		63	86	95

based on the extended T100 index from ERA5. For a comprehensive analysis, we added separate computations for pre-satellite ERA5 data covering DJF 1960–1980.

Table 1 suggests that around 86 % of polar-cap-averaged PCO variations from MLS are related to T100 co-variability. This significantly differs from ERAI, where only slightly more than half of the variability can be attributed. Explained variances for ERA5 starting from DJF 1980 turn out to be substantially higher compared with ERAI and furthermore approach the performance of MLS. The low value for the pre-satellite era in ERA5 suggests that more recent years in reanalyses are much better constrained by observational data. However, it is unclear whether the remaining differences only result from the individual model implementations, assimilation schemes and the quality of the measurements. Instead, e.g., given the growing explained variances for ERA5 with time, the findings may also suggest a much more fundamental change in the interactions between ozone and large-scale atmospheric dynamics. For example, Calvo et al. (2015) showed that stratospheric zonal wind and temperature anomalies during Arctic ozone extremes occurred mainly in recent decades due to substantial anthropogenic ozone-depleting substances, indicating that ozone chemistry has become increasingly important in governing climate variability.

To sum up, we showed that most of the interannual anomalies of polar column ozone in recent years can be attributed to wave-driven anomalous dynamics associated with the varying strength of the polar vortex. Knowledge on the mechanisms that constrain these leading modes of intrinsic ozone variability may help to understand long-term trends in response to external forcings, i.e., due to evolving concentrations of ozone-depleting substances or increased greenhouse gas emissions (e.g., SPARC/IO3C/GAW, 2019). Moreover, feedbacks between anthropogenic climate change and stratospheric dynamics may cause modifications to these modes of variability. Exploring the extent to which ozone itself is involved here would be worth a closer look.

Appendix A: T100 and VT100 predictors for linear regressions

In this study, we used anomaly time series based on polar-cap-averaged zonal-mean temperature at 100 hPa ("T100 index") as the predictors for our linear regression analysis. In Sect. 2, we demonstrated that this index is a suitable measure for the strength of the stratospheric polar vortex. Previous literature on interannual ozone variability often focused on the zonal-mean meridional eddy heat flux $\overline{v'T'}$ at 100 hPa ("VT100 index") to quantify the total available wave driving of the stratosphere. For comparison, Fig. A1 provides additional regression maps for seasonal-mean temperature and ozone from ERA-Interim reanalysis data (December–February, DJF), regressed on both the T100 (DJF) and VT100 (November–January, NDJ) predictors. More details and a discussion of the results are included in Sect. 2.

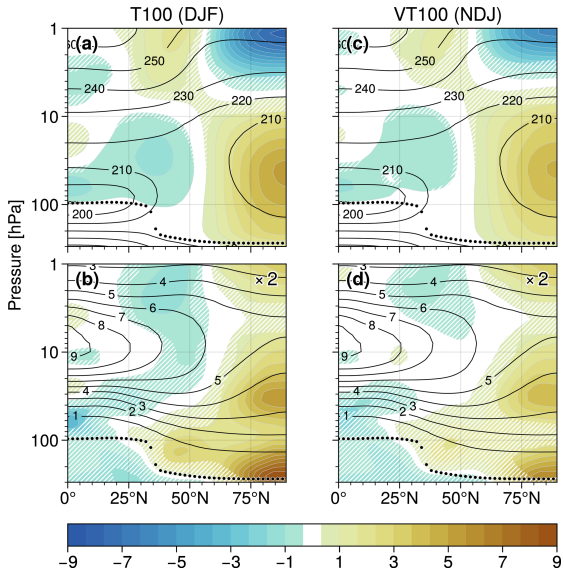

Figure A1. Interannual anomalies (seasonal means, DJF) of zonal-mean temperature (in units of Kelvin, **a** and **c**) and ozone (**b** and **d**), regressed on the T100 index (DJF, **a** and **b**) and the VT100 predictor (NDJ, **c** and **d**), which are both described in Sect. 2. Note the time lag for the VT100 time series. The ozone responses (in percent) are provided relative to the DJF climatology and have been scaled by a factor of 0.5 before plotting. Black contour lines show the corresponding climatologies (in Kelvin and parts per million by volume for temperature and ozone, respectively) and hatches indicate where the regressions are not statistically significant. The thick dotted lines indicate the seasonal-mean thermal tropopause. All results were obtained from ERA-Interim reanalysis data.

Data availability. ERA-Interim data were provided by ECMWF through NCAR. They can also be downloaded from https://apps.ecmwf.int/archive-catalogue/?class=ei (ECMWF, 2023). Aura MLS version 5 data are available at https://disc.gsfc.nasa.gov (Livesey et al., 2022). Data from Hersbach et al. (2019) were downloaded from the Copernicus Climate Change Service (C3S) Climate Data Store. Our study contains modified Copernicus Climate Change Service information 2023. Neither the European Commission nor ECMWF is responsible for any use that may be made of the Copernicus information or data it contains.

Author contributions. FH performed the analyses, supervised by HG and TB. TB initiated the project and processed the ERA-Interim reanalyses. FP provided the MLS observational data. FH wrote the first draft of the paper. All authors contributed in interpreting the results and improving the paper.

Competing interests. The contact author has declared that none of the authors has any competing interests.

Disclaimer. Publisher's note: Copernicus Publications remains neutral with regard to jurisdictional claims in published maps and institutional affiliations.

Acknowledgements. We acknowledge valuable suggestions by two anonymous reviewers that significantly helped to improve this paper. We thank Y. Desille for research on polar vortex–ozone co-variability from modern reanalyses and H. von Heydebrand for extending these studies to chemistry–climate models. We further thank the MLS team for providing the ozone satellite observation data. FH appreciates helpful suggestions by E. Gerber. Throughout this study, we used color codings based on ColorBrewer 2.0 (Brewer, 2022) and Scientific Colour Maps (Crameri et al., 2020; Crameri, 2022). We appreciate the features provided by xarray (Hoyer and Hamman, 2017; Hoyer et al., 2022) and ProPlot (Davis, 2022).

Financial support. This research has been supported by the Deutsche Forschungsgemeinschaft (DFG, German Research Foundation) – TRR 301 – project ID 428312742 ("The tropopause region in a changing atmosphere").

This open-access publication was funded by Ludwig-Maximilians-Universität München.

Review statement. This paper was edited by Gabriele Stiller and reviewed by two anonymous referees.

References

Abalos, M., Legras, B., Ploeger, F., and Randel, W. J.: Evaluating the advective Brewer-Dobson circulation in three reanalyses for the period 1979–2012, J. Geophys. Res.-Atmos., 120, 7534–7554, https://doi.org/10.1002/2015JD023182, 2015.

Adam, O., Grise, K. M., Staten, P., Simpson, I. R., Davis, S. M., Davis, N. A., Waugh, D. W., Birner, T., and Ming, A.: The TropD software package (v1): standardized methods for calculating tropical-width diagnostics, Geosci. Model Dev., 11, 4339–4357, https://doi.org/10.5194/gmd-11-4339-2018, 2018.

Albers, J. R., Perlwitz, J., Butler, A. H., Birner, T., Kiladis, G. N., Lawrence, Z. D., Manney, G. L., Langford, A. O., and Dias, J.: Mechanisms governing interannual variability of stratosphere-to-troposphere ozone transport, J. Geophys. Res.-Atmos., 123, 234–260, https://doi.org/10.1002/2017JD026890, 2018.

Andrews, D. G., Holton, J. R., and Leovy, C. B.: Middle atmosphere dynamics, International Geophysics, vol. 40, Academic Press, ISBN 9780120585762, 1987.

Bahramvash Shams, S., Walden, V. P., Hannigan, J. W., Randel, W. J., Petropavlovskikh, I. V., Butler, A. H., and de la Cámara, A.: Analyzing ozone variations and uncertainties at high latitudes during sudden stratospheric warming events using MERRA-2, Atmos. Chem. Phys., 22, 5435–5458, https://doi.org/10.5194/acp-22-5435-2022, 2022.

Baldwin, M. P., Birner, T., Brasseur, G., Burrows, J., Butchart, N., Garcia, R., Geller, M., Gray, L., Hamilton, K., Harnik, N., Hegglin, M. I., Langematz, U., Robock, A., Sato, K., and Scaife, A. A.: 100 years of progress in understanding the stratosphere and mesosphere, Meteor. Mon., 59, 27.1–27.62, https://doi.org/10.1175/AMSMONOGRAPHS-D-19-0003.1, 2019.

Baldwin, M. P., Ayarzagüena, B., Birner, T., Butchart, N., Butler, A. H., Charlton-Perez, A. J., Domeisen, D. I. V., Garfinkel, C. I., Garny, H., Gerber, E. P., Hegglin, M. I., Langematz, U., and Pedatella, N. M.: Sudden stratospheric warmings, Rev. Geophys., 59, e2020RG000708, https://doi.org/10.1029/2020RG000708, 2021.

Bandoro, J., Solomon, S., Donohoe, A., Thompson, D. W. J., and Santer, B. D.: Influences of the Antarctic ozone hole on southern hemispheric summer climate change, J. Climate, 27, 6245–6264, https://doi.org/10.1175/JCLI-D-13-00698.1, 2014.

Barnes, P. W., Robson, T. M., Neale, P. J., Williamson, C. E., Zepp, R. G., Madronich, S., Wilson, S. R., Andrady, A. L., Heikkilä, A. M., Bernhard, G. H., Bais, A. F., Neale, R. E., Bornman, J. F., Jansen, M. A. K., Klekociuk, A. R., Martinez-Abaigar, J., Robinson, S. A., Wang, Q.-W., Banaszak, A. T., Häder, D.-P., Hylander, S., Rose, K. C., Wängberg, S.-Å., Foereid, B., Hou, W.-C., Ossola, R., Paul, N. D., Ukpebor, J. E., Andersen, M. P. S., Longstreth, J., Schikowski, T., Solomon, K. R., Sulzberger, B., Bruckman, L. S., Pandey, K. K., White, C. C., Zhu, L., Zhu, M., Aucamp, P. J., Liley, J. B., McKenzie, R. L., Berwick, M., Byrne, S. N., Hollestein, L. M., Lucas, R. M., Olsen, C. M., Rhodes, L. E., Yazar, S., and Young, A. R.: Environmental effects of stratospheric ozone depletion, UV radiation, and interactions with climate change: UNEP Environmental Effects Assessment Panel, Update 2021, Photochem. Photobiol. S., 21, 275–301, https://doi.org/10.1007/s43630-022-00176-5, 2022.

Bell, B., Hersbach, H., Simmons, A., Berrisford, P., Dahlgren, P., Horányi, A., Muñoz-Sabater, J., Nicolas, J., Radu, R., Schepers, D., Soci, C., Villaume, S., Bidlot, J.-R., Haimberger, L., Woollen, J., Buontempo, C., and Thépaut, J.-N.: The ERA5 global reanalysis: preliminary extension to 1950, Q. J. Roy. Meteor. Soc., 147, 4186–4227, https://doi.org/10.1002/qj.4174, 2021.

Benito-Barca, S., Calvo, N., and Abalos, M.: Driving mechanisms for the El Niño–Southern Oscillation impact on stratospheric ozone, Atmos. Chem. Phys., 22, 15729–15745, https://doi.org/10.5194/acp-22-15729-2022, 2022.

Brasseur, G. P. and Solomon, S.: Aeronomy of the middle atmosphere. Chemistry and physics of the stratosphere and mesosphere, 3rd edn., Springer Dordrecht, https://doi.org/10.1007/1-4020-3824-0, 2005.

Brewer, C. A.: ColorBrewer 2.0, https://colorbrewer2.org (last access: 6 September 2023), 2022.

Butchart, N.: The Brewer-Dobson circulation, Rev. Geophys., 52, 157–184, https://doi.org/10.1002/2013RG000448, 2014.

Butler, A. H., Sjoberg, J. P., Seidel, D. J., and Rosenlof, K. H.: A sudden stratospheric warming compendium, Earth Syst. Sci. Data, 9, 63–76, https://doi.org/10.5194/essd-9-63-2017, 2017.

Calvo, N., Polvani, L. M., and Solomon, S.: On the surface impact of Arctic stratospheric ozone extremes, Environ. Res. Lett., 10, 094003, https://doi.org/10.1088/1748-9326/10/9/094003, 2015.

Chiodo, G. and Polvani, L. M.: Reduced southern hemispheric circulation response to quadrupled CO_2 due to stratospheric ozone feedback, Geophys. Res. Lett., 44, 465–474, https://doi.org/10.1002/2016GL071011, 2017.

Chiodo, G. and Polvani, L. M.: The response of the ozone layer to quadrupled CO_2 concentrations: implications for climate, J. Climate, 32, 7629–7642, https://doi.org/10.1175/JCLI-D-19-0086.1, 2019.

Chiodo, G., Polvani, L. M., Marsh, D. R., Stenke, A., Ball, W., Rozanov, E., Muthers, S., and Tsigaridis, K.: The response of the ozone layer to quadrupled CO_2 concentrations, J. Climate, 31, 3893–3907, https://doi.org/10.1175/JCLI-D-17-0492.1, 2018.

Crameri, F.: Scientific colour maps, Zenodo [code], https://doi.org/10.5281/zenodo.1243862, 2022.

Crameri, F., Shephard, G. E., and Heron, P. J.: The misuse of colour in science communication, Nat. Commun., 11, 5444, https://doi.org/10.1038/s41467-020-19160-7, 2020.

Davis, L. L. B.: ProPlot, Zenodo [code], https://doi.org/10.5281/zenodo.3873878, 2022.

Davis, S. M., Hegglin, M. I., Dragani, R., Fujiwara, M., Harada, Y., Kobayashi, C., Long, C., Manney, G. L., Nash, E. R., Potter, G. L., Tegtmeier, S., Wang, T., Wargan, K., and Wright, J. S.: Overview of ozone and water vapour, in: SPARC Reanalysis Intercomparison Project (S-RIP) Final Report, edited by: Fujiwara, M., Manney, G. L., Gray, L. J., and Wright, J. S., SPARC Report No. 10, WCRP-6/2021, 123–164, https://doi.org/10.17874/800dee57d13, 2022.

de la Cámara, A., Abalos, M., and Hitchcock, P.: Changes in stratospheric transport and mixing during sudden stratospheric warmings, J. Geophys. Res.-Atmos., 123, 3356–3373, https://doi.org/10.1002/2017JD028007, 2018a.

de la Cámara, A., Abalos, M., Hitchcock, P., Calvo, N., and Garcia, R. R.: Response of Arctic ozone to sudden stratospheric warmings, Atmos. Chem. Phys., 18, 16499–16513, https://doi.org/10.5194/acp-18-16499-2018, 2018b.

Dee, D. P., Uppala, S. M., Simmons, A. J., Berrisford, P., Poli, P., Kobayashi, S., Andrae, U., Balmaseda, M. A., Balsamo, G., Bauer, P., Bechtold, P., Beljaars, A. C. M., van de Berg, L., Bidlot, J., Bormann, N., Delsol, C., Dragani, R., Fuentes, M., Geer, A. J., Haimberger, L., Healy, S. B., Hersbach, H., Hólm, E. V., Isaksen, L., Kållberg, P., Köhler, M., Matricardi, M., McNally, A. P., Monge-Sanz, B. M., Morcrette, J.-J., Park, B.-K., Peubey, C., de Rosnay, P., Tavolato, C., Thépaut, J.-N., and Vitart, F.: The ERA-Interim reanalysis: configuration and performance of the data assimiliation system, Q. J. Roy. Meteor. Soc., 137, 553–597, https://doi.org/10.1002/qj.828, 2011.

Dietmüller, S., Ponater, M., and Sausen, R.: Interactive ozone induces a negative feedback in CO_2-driven climate change simulations, J. Geophys. Res.-Atmos., 119, 1796–1805, https://doi.org/10.1002/2013JD020575, 2014.

Domeisen, D. I. V., Butler, A. H., Charlton-Perez, A. J., Ayarzagüena, B., Baldwin, M. P., Dunn-Sigouin, E., Furtado, J. C., Garfinkel, C. I., Hitchcock, P., Karpechko, A. Y., Kim, H., Knight, J., Lang, A. L., Lim, E.-P., Marshall, A., Roff, G., Schwartz, C., Simpson, I. R., Son, S.-W., and Taguchi, M.: The role of the stratosphere in subseasonal to seasonal prediction: 2. Predictability arising from stratosphere-troposphere coupling, J. Geophys. Res.-Atmos., 125, e2019JD030923, https://doi.org/10.1029/2019JD030923, 2020.

Dragani, R.: On the quality of the ERA-Interim ozone reanalyses: comparisons with satellite data, Q. J. Roy. Meteor. Soc., 137, 1312–1326, https://doi.org/10.1002/qj.821, 2011.

ECMWF: Archive Catalogue, European Centre for Medium-Range Weather Forecasts [data set], https://apps.ecmwf.int/archive-catalogue/?class=ei (last access: 6 September 2023), 2023.

Friedel, M., Chiodo, G., Stenke, A., Domeisen, D. I. V., Fueglistaler, S., Anet, J. G., and Peter, T.: Springtime Arctic ozone depletion forces northern hemisphere climate anomalies, Nat. Geosci., 15, 541–547, https://doi.org/10.1038/s41561-022-00974-7, 2022a.

Friedel, M., Chiodo, G., Stenke, A., Domeisen, D. I. V., and Peter, T.: Effects of Arctic ozone on the stratospheric spring onset and its surface impact, Atmos. Chem. Phys., 22, 13997–14017, https://doi.org/10.5194/acp-22-13997-2022, 2022b.

Fu, Q., Solomon, S., and Lin, P.: On the seasonal dependence of tropical lower-stratospheric temperature trends, Atmos. Chem. Phys., 10, 2643–2653, https://doi.org/10.5194/acp-10-2643-2010, 2010.

Fusco, A. C. and Salby, M. L.: Interannual variations of total ozone and their relationship to variations of planetary wave activity, J. Climate, 12, 1619–1629, https://doi.org/10.1175/1520-0442(1999)012<1619:IVOTOA>2.0.CO;2, 1999.

Garcia, R. R. and Hartmann, D. L.: The role of planetary waves in the maintenance of the zonally averaged ozone distribution of the upper stratosphere, J. Atmos. Sci., 37, 2248–2264, https://doi.org/10.1175/1520-0469(1980)037<2248:TROPWI>2.0.CO;2, 1980.

Gettelman, A., Hoor, P., Pan, L. L., Randel, W. J., Hegglin, M. I., and Birner, T.: The extratropical upper troposphere and lower stratosphere, Rev. Geophys., 49, RG3003, https://doi.org/10.1029/2011RG000355, 2011.

Grise, K. M., Thompson, D. W. J., and Birner, T.: A global survey of static stability in the stratosphere and upper troposphere, J. Cli-

mate, 23, 2275–2292, https://doi.org/10.1175/2009JCLI3369.1, 2010.

Hartmann, D. L. and Garcia, R. R.: A mechanistic model of ozone transport by planetary waves in the stratosphere, J. Atmos. Sci., 36, 350–364, https://doi.org/10.1175/1520-0469(1979)036<0350:AMMOOT>2.0.CO;2, 1979.

Haynes, P. H., McIntyre, M. E., Shepherd, T. G., Marks, C. J., and Shine, K. P.: On the "downward control" of extratropical diabatic circulations by eddy-induced mean zonal forces, J. Atmos. Sci., 48, 651–678, https://doi.org/10.1175/1520-0469(1991)048<0651:OTCOED>2.0.CO;2, 1991.

Hersbach, H., Bell, B., Berrisford, P., Biavati, G., Horányi, A., Muñoz-Sabater, J., Nicolas, J., Peubey, C., Radu, R., Rozum, I., Schepers, D., Simmons, A., Soci, C., Dee, D., and Thépaut, J.-N.: ERA5 monthly averaged data on pressure levels from 1959 to present, Copernicus Climate Change Service (C3S) Climate Data Store (CDS), https://doi.org/10.24381/cds.6860a573, 2019.

Hersbach, H., Bell, B., Berrisford, P., Hirahara, S., Horányi, A., Muñoz-Sabater, J., Nicolas, J., Peubey, C., Radu, R., Schepers, D., Simmons, A., Soci, C., Abdalla, S., Abellan, X., Balsamo, G., Bechtold, P., Biavati, G., Bidlot, J., Bonavita, M., de Chiara, G., Dahlgren, P., Dee, D., Diamantakis, M., Dragani, R., Flemming, J., Forbes, R., Fuentes, M., Geer, A., Haimberger, L., Healy, S., Hogan, R. J., Hólm, E., Janisková, M., Keeley, S., Laloyaux, P., Lopez, P., Lupu, C., Radnoti, G., de Rosnay, P., Rozum, I., Vamborg, F., Villaume, S., and Thépaut, J.-N.: The ERA5 global reanalysis, Q. J. Roy. Meteor. Soc., 146, 1999–2049, https://doi.org/10.1002/qj.3803, 2020.

Hitchcock, P., Shepherd, T. G., and Yoden, S.: On the approximation of local and linear radiative damping in the middle atmosphere, J. Atmos. Sci., 67, 2070–2085, https://doi.org/10.1175/2009JAS3286.1, 2010.

Hong, H.-J. and Reichler, T.: Local and remote response of ozone to Arctic stratospheric circulation extremes, Atmos. Chem. Phys., 21, 1159–1171, https://doi.org/10.5194/acp-21-1159-2021, 2021.

Hoyer, S. and Hamman, J. J.: xarray: N-D labeled arrays and datasets in Python, Journal of Open Research Software, 5, 10, https://doi.org/10.5334/jors.148, 2017.

Hoyer, S., Roos, M., Hamman, J., Magin, J., Cherian, D., Fitzgerald, C., Hauser, M., Fujii, K., Maussion, F., Imperiale, G., Clark, S., Kleeman, A., Nicholas, T., Kluyver, T., Westling, J., Munroe, J., Amici, A., Barghini, A., Banihirwe, A., Bell, R., Hatfield-Dodds, Z., Abernathey, R., Bovy, B., Omotani, J., Mühlbauer, K., Roszko, M. K., and Wolfram, P. J.: xarray, Zenodo [code], https://doi.org/10.5281/zenodo.598201, 2022.

IPCC: Climate change 2021: The physical science basis: Contribution of working group I to the sixth assessment report of the Intergovernmental Panel on Climate Change, Cambridge University Press, https://doi.org/10.1017/9781009157896, 2021.

Ivy, D. J., Solomon, S., Calvo, N., and Thompson, D. W. J.: Observed connections of Arctic stratospheric ozone extremes to northern hemisphere surface climate, Environ. Res. Lett., 12, 024004, https://doi.org/10.1088/1748-9326/aa57a4, 2017.

Kinnersley, J. S. and Tung, K.-K.: Modeling the global interannual variability of ozone due to the equatorial QBO and to extratropical planetary wave variability, J. Atmos. Sci., 55, 1417–1428, https://doi.org/10.1175/1520-0469(1998)055<1417:MTGIVO>2.0.CO;2, 1998.

Konopka, P., Grooß, J.-U., Plöger, F., and Müller, R.: Annual cycle of horizontal in-mixing into the lower tropical stratosphere, J. Geophys. Res., 114, D19111, https://doi.org/10.1029/2009JD011955, 2009.

Lait, L. R.: An alternative form for potential vorticity, J. Atmos. Sci., 51, 1754–1759, https://doi.org/10.1175/1520-0469(1994)051<1754:AAFFPV>2.0.CO;2, 1994.

Leovy, C. B., Sun, C.-R., Hitchman, M. H., Remsberg, E. E., Russell III, J. M., Gordley, L. L., Gille, J. C., and Lyjak, L. V.: Transport of ozone in the middle stratosphere: evidence for planetary wave breaking, J. Atmos. Sci., 42, 230–244, https://doi.org/10.1175/1520-0469(1985)042<0230:TOOITM>2.0.CO;2, 1985.

Livesey, N. J., Read, W. G., Wagner, P. A., Froidevaux, L., Santee, M. L., Schwartz, M. J., Lambert, A., Millán Valle, L. F., Pumphrey, H. C., Manney, G. L., Fuller, R. A., Jarnot, R. F., Knosp, B. W., and Lay, R. R.: Earth Observing System (EOS) Aura Microwave Limb Sounder (MLS) version 5.0x level 2 and 3 data quality and description document, Version 5.0–1.1a, JPL D-105336 Rev. B, https://disc.gsfc.nasa.gov (last access: 6 September 2023), 2022.

Lubis, S. W., Silverman, V., Matthes, K., Harnik, N., Omrani, N.-E., and Wahl, S.: How does downward planetary wave coupling affect polar stratospheric ozone in the Arctic winter stratosphere?, Atmos. Chem. Phys., 17, 2437–2458, https://doi.org/10.5194/acp-17-2437-2017, 2017.

Ma, J., Waugh, D. W., Douglass, A. R., Kawa, S. R., Newman, P. A., Pawson, S., Stolarski, R., and Lin, S. J.: Interannual variability of stratospheric trace gases: the role of extratropical wave driving, Q. J. Roy. Meteor. Soc., 130, 2459–2474, https://doi.org/10.1256/qj.04.28, 2004.

Match, A. and Gerber, E. P.: Tropospheric expansion under global warming reduces tropical lower stratospheric ozone, Geophys. Res. Lett., 49, e2022GL099463, https://doi.org/10.1029/2022GL099463, 2022.

Monge-Sanz, B. M., Birner, T., Chabrillat, S., Diallo, M., Haenel, F., Konopka, P., Legras, B., Ploeger, F., Reddmann, T., Stiller, G., Wright, J. S., Abalos, M., Boenisch, H., Davis, S., Garny, H., Hitchcock, P., Miyazaki, K., Roscoe, H. K., Sato, K., Tao, M., and Waugh, D.: Brewer-Dobson circulation, in: SPARC Reanalysis Intercomparison Project (S-RIP) Final Report, edited by: Fujiwara, M., Manney, G. L., Gray, L. J., and Wright, J. S., SPARC Report No. 10, WCRP-6/2021, 165–220, https://doi.org/10.17874/800dee57d13, 2022.

Newman, P. A., Nash, E. R., and Rosenfield, J. E.: What controls the temperature of the Arctic stratosphere during the spring?, J. Geophys. Res.-Atmos., 106, 19999–20010, https://doi.org/10.1029/2000JD000061, 2001.

Nowack, P. J., Abraham, N. L., Maycock, A. C., Braesicke, P., Gregory, J. M., Joshi, M. M., Osprey, A., and Pyle, J. A.: A large ozone-circulation feedback and its implications for global warming assessments, Nat. Clim. Change, 5, 41–45, https://doi.org/10.1038/nclimate2451, 2015.

Nowack, P. J., Abraham, N. L., Braesicke, P., and Pyle, J. A.: The impact of stratospheric ozone feedbacks on climate sensitivity estimates, J. Geophys. Res.-Atmos., 123, 4630–4641, https://doi.org/10.1002/2017JD027943, 2018.

Plumb, R. A.: Stratospheric transport, J. Meteorol. Soc. Jpn. Ser. II, 80, 793–809, https://doi.org/10.2151/jmsj.80.793, 2002.

Polvani, L. M. and Waugh, D. W.: Upward wave activity flux as a precursor to extreme stratospheric events and subsequent anomalous surface weather regimes, J. Climate, 17, 3548–3554, https://doi.org/10.1175/1520-0442(2004)017<3548:UWAFAA>2.0.CO;2, 2004.

Randel, W. J., Wu, F., and Stolarski, R.: Changes in column ozone correlated with the stratospheric EP flux, J. Meteorol. Soc. Jpn., 80, 849–862, https://doi.org/10.2151/jmsj.80.849, 2002.

Smith, K. L. and Polvani, L. M.: The surface impacts of Arctic stratospheric ozone anomalies, Environ. Res. Lett., 9, 074015, https://doi.org/10.1088/1748-9326/9/7/074015, 2014.

Son, S.-W., Tandon, N. F., and Polvani, L. M.: The fine-scale structure of the global tropopause derived from COSMIC GPS radio occultation measurements, J. Geophys. Res.-Atmos., 116, D20113, https://doi.org/10.1029/2011JD016030, 2011.

Son, S.-W., Purich, A., Hendon, H. H., Kim, B.-M., and Polvani, L. M.: Improved seasonal forecast using ozone hole variability?, Geophys. Res. Lett., 40, 6231–6235, https://doi.org/10.1002/2013GL057731, 2013.

SPARC/IO3C/GAW: SPARC/IO3/GAW report on long-term ozone trends and uncertainties in the stratosphere: SPARC Report No. 9, GAW Report No. 241, WCRP-17/2018, https://doi.org/10.17874/f899e57a20b, 2019.

Strahan, S. E., Douglass, A. R., and Steenrod, S. D.: Chemical and dynamical impacts of stratospheric sudden warmings on Arctic ozone variability, J. Geophys. Res.-Atmos., 121, 11836–11851, https://doi.org/10.1002/2016JD025128, 2016.

Tung, K. K.: Nongeostrophic theory of zonally averaged circulation. Part I: Formulation, J. Atmos. Sci., 43, 2600–2618, https://doi.org/10.1175/1520-0469(1986)043<2600:NTOZAC>2.0.CO;2, 1986.

von Heydebrand, H.: Interannual ozone variability in the Northern Hemisphere from coupled chemistry–climate models, Bachelor's thesis, Faculty of Physics, Ludwig-Maximilians-Universität München, Munich, Germany, 2022.

Wargan, K. and Coy, L.: Strengthening of the tropopause inversion layer during the 2009 sudden stratospheric warming: a MERRA-2 study, J. Atmos. Sci., 73, 1871–1887, https://doi.org/10.1175/JAS-D-15-0333.1, 2016.

Waters, J. W., Froidevaux, L., Harwood, R. S., Jarnot, R. F., Pickett, H. M., Read, W. G., Siegel, P. H., Cofield, R. E., Filipiak, M. J., Flower, D. A., Holden, J. R., Lau, G. K., Livesey, N. J., Manney, G. L., Pumphrey, H. C., Santee, M. L., Wu, D. L., Cuddy, D. T., Lay, R. R., Loo, M. S., Perun, V. S., Schwartz, M. J., Stek, P. C., Thurstans, R. P., Boyles, M. A., Chandra, K. M., Chavez, M. C., Chen, G.-S., Chudasama, B. V., Dodge, R., Fuller, R. A., Girard, M. A., Jiang, J. H., Jiang, Y., Knosp, B. W., LaBelle, R. C., Lam, J. C., Lee, K. A., Miller, D., Oswald, J. E., Patel, N. C., Pukala, D. M., Quintero, O., Scaff, D. M., van Snyder, W., Tope, M. C., Wagner, P. A., and Walch, M. J.: The Earth observing system microwave limb sounder (EOS MLS) on the aura satellite, IEEE T. Geosci. Remote, 44, 1075–1092, https://doi.org/10.1109/TGRS.2006.873771, 2006.

Weber, M., Dhomse, S., Wittrock, F., Richter, A., Sinnhuber, B.-M., and Burrows, J. P.: Dynamical control of NH and SH winter/spring total ozone from GOME observations in 1995–2002, Geophys. Res. Lett., 30, 1583, https://doi.org/10.1029/2002GL016799, 2003.

Weber, M., Dikty, S., Burrows, J. P., Garny, H., Dameris, M., Kubin, A., Abalichin, J., and Langematz, U.: The Brewer-Dobson circulation and total ozone from seasonal to decadal time scales, Atmos. Chem. Phys., 11, 11221–11235, https://doi.org/10.5194/acp-11-11221-2011, 2011.

WMO: Meteorology – a three-dimensional science: Second session of the Commission for Aerology, WMO Bulletin, 6, 134–138, 1957.

WMO: Scientific assessment of ozone depletion: 2022, GAW Report No. 278, Geneva, https://ozone.unep.org (last access: 6 September 2023), 2022.

Young, P. J., Rosenlof, K. H., Solomon, S., Sherwood, S. C., Fu, Q., and Lamarque, J.-F.: Changes in stratospheric temperatures and their implications for changes in the Brewer-Dobson circulation, 1979–2005, J. Climate, 25, 1759–1772, https://doi.org/10.1175/2011JCLI4048.1, 2012.